AGU PUBLICATIONS

Paleoceanography

RESEARCH ARTICLE
10.1002/2015PA002802

Key Points:
- Reconstruction of surface conditions off the Sunda Strait over the past 40 kyr
- Fresher surface condition during the Holocene compared to last glacial
- Java Sea waters have contributed to hydrology change off the Sunda Strait

Supporting Information:
- Tables S1–S3

Correspondence to:
R. Y. Setiawan,
riza.y.setiawan@gmail.com

Citation:
Setiawan, R. Y., M. Mohtadi, J. Southon, J. Groeneveld, S. Steinke, and D. Hebbeln (2015), The consequences of opening the Sunda Strait on the hydrography of the eastern tropical Indian Ocean, *Paleoceanography*, *30*, 1358–1372, doi:10.1002/2015PA002802.

Received 10 MAR 2015
Accepted 31 AUG 2015
Accepted article online 7 OCT 2015
Published online 31 OCT 2015

The consequences of opening the Sunda Strait on the hydrography of the eastern tropical Indian Ocean

Riza Yuliratno Setiawan[1,2], Mahyar Mohtadi[1], John Southon[3], Jeroen Groeneveld[1,4], Stephan Steinke[1], and Dierk Hebbeln[1]

[1]MARUM – Center for Marine Environmental Sciences, University of Bremen, Bremen, Germany, [2]Now at Department of Marine Sciences, Diponegoro University, Indonesia, [3]Earth System Science Department, University of California, Irvine, California, USA, [4]Alfred-Wegener Institute, Helmholtz Center for Polar and Marine Research, Potsdam, Germany

Abstract The advection of relatively fresh Java Sea water through the Sunda Strait is presently responsible for the low-salinity "tongue" in the eastern tropical Indian Ocean with salinities as low as 32‰. The evolution of the hydrologic conditions in the eastern tropical Indian Ocean since the last glacial period, when the Sunda shelf was exposed and any advection via the Sunda Strait was cutoff, and the degree to which these conditions were affected by the Sunda Strait opening are not known. Here we have analyzed two sediment cores (GeoB 10042–1 and GeoB 10043–3) collected from the eastern tropical Indian Ocean off the Sunda Strait that cover the past ~40,000 years. We investigate the magnitude of terrigenous supply, sea surface temperature (SST), and seawater $\delta^{18}O$ ($\delta^{18}O_{sw}$) changes related to the sea level-driven opening of the Sunda Strait. Our new spliced records off the Sunda Strait show that during the last glacial, average SST was cooler and $\delta^{18}O_{sw}$ was higher than elsewhere in the eastern tropical Indian Ocean. Seawater $\delta^{18}O$ decreased ~0.5‰ after the opening of the Sunda Strait at ~10 kyr B.P. accompanied by an SST increase of 1.7°C. We suggest that fresher sea surface conditions have persisted ever since due to a continuous transport of low-salinity Java Sea water into the eastern tropical Indian Ocean via the Sunda Strait that additionally increased marine productivity through the concomitant increase in terrigenous supply.

1. Introduction

The Sunda Shelf in the Indo-Pacific Warm Pool (IPWP) is one of the largest shelves in the world with less than 70 m water depth. During the Last Glacial Maximum (LGM), when global sea level was ~130 m below the present level, the wide Sunda Shelf was exposed forming a huge land mass also known as Sundaland [*Tjia,* 1980; *Pelejero et al.,* 1999; *Hanebuth et al.,* 2000]. Model results suggest that the exposure of the Sunda Shelf altered the atmospheric circulation by weakening the Indian Ocean Walker Circulation, which was accompanied by increased aridity in the eastern tropical Indian Ocean and higher sea surface salinity (SSS) south of Java [*DiNezio and Tierney*, 2013].

Marine and terrestrial proxy data suggest that the Sunda Shelf was flooded at ~9.5 kyr B.P. due to eustatic sea level rise [*Hanebuth et al.,* 2000, 2011; *Griffiths et al.,* 2009, 2013; *Linsley et al.,* 2010]. The flooding of the shelf has been suggested to affect seawater $\delta^{18}O$ and rainfall in regions to the east and southeast of the Sunda Shelf, in the Timor Sea [*Xu et al.,* 2008] and the Savu Sea [*Dubois et al.,* 2014], in Flores [*Griffiths et al.,* 2009, 2013], and in the Makassar Strait [*Linsley et al.,* 2010]. However, temperature and rainfall proxy records from Sulawesi [*Russell et al.,* 2014] and from sites to the west and north of the Sunda Shelf do not show a sea level-related variability on glacial-interglacial timescales; e.g., in Borneo [*Carolin et al.,* 2013; *Dubois et al.,* 2014] and western Sumatra [*Maloney*, 1980; *Mohtadi et al.,* 2014; *Niedermeyer et al.,* 2014; *Stuijts et al.,* 1988; *van der Kaars et al.,* 2010]. Records from south of the Sunda Shelf are equivocal [*Kershaw et al.,* 2007; *Mohtadi et al.,* 2011a]. Moreover, some results suggest that the flooding of the Sunda Shelf influenced the Indonesian Throughflow (ITF) by changing a surface-dominated to a thermocline-dominated flow [*Linsley et al.,* 2010; *Xu et al.,* 2008]. In the absence of any influence of the relatively fresh South China Sea (SCS) water, that today adds to the ITF through the Java Sea, glacial ITF transport was dominated by warmer and saltier surface flow [*Xu et al.,* 2008].

The effect of the Sunda Shelf flooding and the opening of the Sunda Strait at ~9.5 kyr B.P. on the hydrology of the eastern tropical Indian Ocean is not well known. Presently, the Sunda Strait is the most important link

between the Java Sea and the Indian Ocean as it transports warm, low-salinity Java Sea water into the eastern tropical Indian Ocean [*Putri*, 2005]. This advection of relatively fresh water has significant impacts particularly on the upper ocean stratification in the eastern tropical Indian Ocean off the Sunda Strait [*Putri*, 2005; *Du and Qu*, 2010]. Data from a sedimentary record to the northwest of the Sunda Strait imply that during periods of lower sea level prior to the Holocene the input of less saline waters via the Sunda Strait was cutoff and saltier sea surface condition prevailed in the eastern tropical Indian Ocean [*Mohtadi et al.,* 2010a, 2010b]. Here we study two additional marine sedimentary archives collected in the eastern tropical Indian Ocean off the Sunda Strait with a higher temporal resolution and more accurate age model for the past 40 kyr to understand the influence of an exposed or a flooded Sunda Shelf on the regional hydrology. Records of bulk sedimentary element composition together with stable oxygen isotope ($\delta^{18}O$) and Mg/Ca ratio of the planktic foraminifera *Globigerinoides ruber* in a strict sense are used to unravel changes in the regional hydrology of the eastern tropical Indian Ocean related to sea level changes and the resulting exposure/flooding of the Sunda Shelf.

2. Study Area

Today the eastern tropical Indian Ocean is greatly influenced by the Australian-Indonesian monsoon system. The dynamics of the seasonally reversing monsoon winds over the study area impacts oceanic circulation, sea surface temperature (SST), and SSS along the southern coasts of Java and Sumatra [*Susanto et al.,* 2001; *Qu and Meyers*, 2005; *Du et al.,* 2005, 2008]. During the northwest monsoon (NWM) season (December–February), winds blow from the Eurasian continent, pass the South China Sea and the Bay of Bengal, and carry warm and moist air to Indonesia [*Gordon*, 2005; *Qu et al.,* 2005]. Along the coasts of Sumatra and Java, the almost year-round eastward flowing South Java Current carries low-salinity, warm water from the eastern equatorial Indian Ocean off Sumatra into the southeast Indian Ocean [*Du et al.,* 2005; *Sprintall et al.,* 2009, 2010]. The direction of the South Java Current (SJC) is reversed only during the southeast monsoon (SEM) season (June–September), carrying higher-salinity water flows westward [*Sprintall et al.,* 2010] (Figure 1a). During this time southeasterly winds blow from Australia and carry warm and dry air to Indonesia [*Gordon*, 2005; *Qu et al.,* 2005]. A striking feature during the SEM is the appearance of wind-induced upwelling centered south of Java [*Susanto et al.,* 2001].

The eastern tropical Indian Ocean is a region where precipitation (P) exceeds evaporation (E) throughout the year [*Hendon*, 2003]. Moreover, *Qu and Meyers* [2005] suggest that a large P-E difference is confined to the coastal region of Indonesia, with a maximum $>10\ mm\ day^{-1}$ occurring near the coast of Sumatra. This large P-E creates a strong salinity-induced stratification in the surface waters. Further south in the monsoon region of southern Indonesia, the rainy season is principally linked to the NWM due to the southward progression of the Intertropical Convergence Zone (ITCZ), while the dry season peaks during the SEM [*Aldrian and Susanto*, 2003; *Hendon*, 2003].

Another important oceanic circulation component in the study area is the ITF. The ITF transports Pacific Ocean water into the Indian Ocean via multiple passages within the Indonesian Seas [*Vranes and Gordon*, 2005; *Gordon et al.,* 2010]. Presently, the estimated transport is ~15 sverdrup ($1\ Sv = 10^6\ m^3\ s^{-1}$) and roughly 80% of that is transported via the main pathway, the Makassar Strait [*Gordon et al.,* 2010]. The ITF modifies the heat and freshwater budgets and air-sea heat fluxes of the Pacific and Indian Oceans and may play a role in ENSO and Asian monsoon climate phenomena [*Gordon et al.,* 2003]. The relatively cool and fresh ITF exits the Indonesian Seas through Timor Passage, Lombok, and Ombai Straits and flows westward across the Indian Ocean near 12°S [*Gordon et al.,* 2010].

Modern oceanographic observations show that the Java Sea water, characterized by low-salinity and high-temperature waters, is the dominant water mass passing through the Sunda Strait continuously during the entire year [*Putri*, 2005]. Moreover, a recent modeling study suggests that from the annual mean southward transport of 0.6 Sv through the Karimata Strait [*Gordon et al*., 2012], about 0.5 Sv passes later on through the Sunda Strait [*Du and Qu*, 2010]. Combined with runoff from Java and Sumatra, this transport is responsible for the low-salinity "tongue" in the SJC with salinities as low as 32‰ (Figure 1) [*Wijffels et al*., 1996], which can extend as far as 13°S [*Gingele et al.,* 2002; *Ding et al.,* 2006]. The large amount of freshwater in this region results in the development of a thick barrier layer, a layer that separates the base of the mixed layer from the thermocline. The presence of the barrier layer in the study area impedes the intrusion of thermocline waters to the mixed layer during the upwelling season and reduces its effect on the SST [e.g., *Du et al.,* 2005].

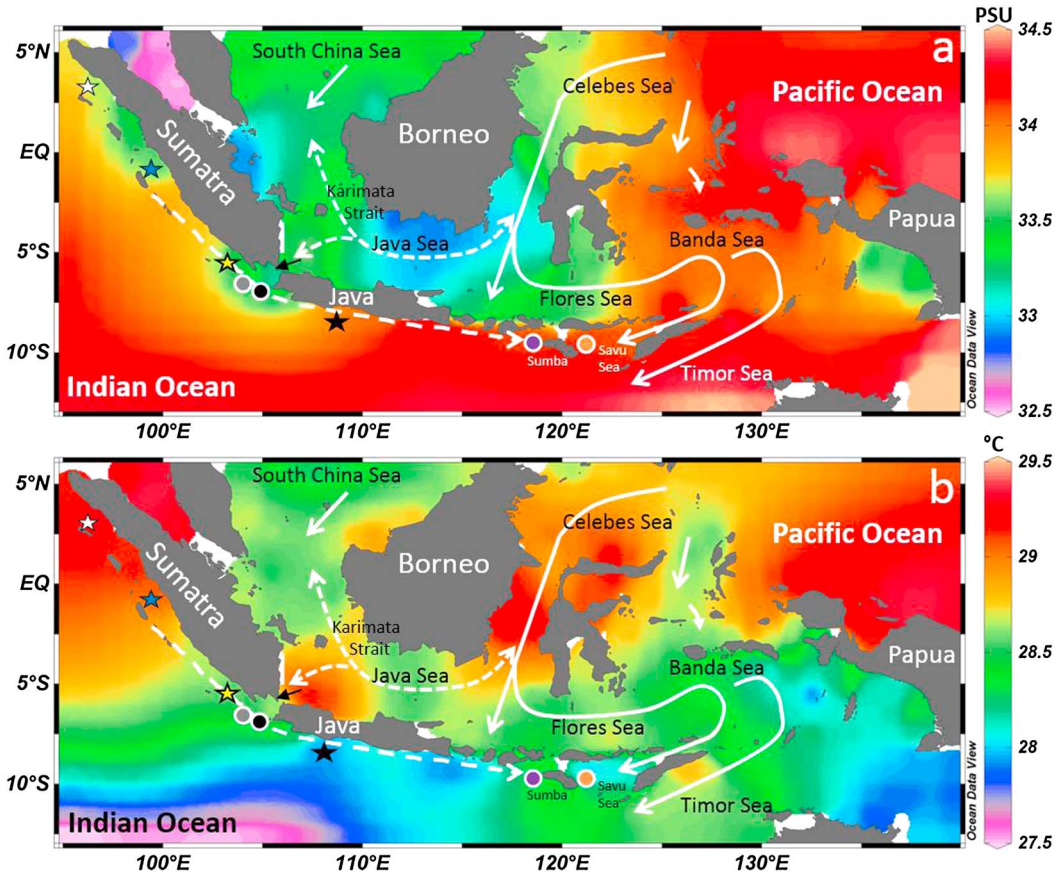

Figure 1. Annual mean maps of (a) sea surface salinity (psu) [*Zweng et al.,* 2013] and (b) sea surface temperature (°C) [*Locarnini et al.,* 2013] obtained from the World Ocean Atlas 2013. The Sunda Strait is indicated by black arrow in the maps. Grey, black, purple, and orange dots denote the positions of GeoB 10042–1 and GeoB 10043–3 (this study), MD98-2165 [*Levi et al.,* 2007], and GeoB 10069–3 [*Gibbons et al.,* 2014], respectively. White, blue, yellow, and black stars show the positions of SO189-119KL, SO189-39KL [*Mohtadi et al.,* 2014], GeoB 10038–4 [*Mohtadi et al.,* 2010a, 2010b], and sediment trap JAM1-3 [*Mohtadi et al.,* 2009]. White dashed arrows in the Java Sea and off the southern Sumatra and Java depict the movement of low-salinity water and the direction of the South Java Current [*Sprintall et al.,* 2010]. White solid lines denote ITF pathways.

3. Materials and Method

3.1. Sediment Cores GeoB 10042–1 and GeoB 10043–3

The two gravity cores GeoB 10042–1 (7°06.81′S 104° 38.58′E, 2454 m water depth, core length: 540 cm) and GeoB 10043–3 (7°18.57′S 105° 03.53′E, 2171 m water depth, core length: 390 cm) were collected from west of the Sunda Strait during the SO-184 field campaign with the German RV SONNE in 2005 (Figure 1) [*Hebbeln,* 2006]. Both cores, GeoB 10042–1 and GeoB 10043–3, consist of nannofossil ooze. In core GeoB 10043–3 a turbidite layer is observed from 225 to 232 cm depth.

3.2. Radiocarbon Dating

For radiocarbon dating the surface-dwelling planktic foraminifera species *Globigerinoides ruber* in a strict sense and *Globigerinoides sacculifer* (without the sac-like final chamber) were handpicked under a binocular microscope from the >150 μm fraction. The abundance of these species within the cores was generally low, and occasionally, both species were combined to obtain a sufficient amount of datable material. Samples were then measured at the Keck Carbon Cycle Accelerator Mass Spectrometry Laboratory, University of California, Irvine. Raw ^{14}C ages were converted to 2σ calendar ages with the CALIB 7.0 software using the Marine13 calibration data set [*Reimer et al.,* 2013] (Table 1) with a regional reservoir correction of 100 years [*Southon et al.,* 2013].

Table 1. AMS ^{14}C and Calendar Ages Obtained From Planktic Foraminifera Shells in Cores GeoB 10042–1 and GeoB 10043–3[a]

UCIAMS #	Depth (cm)	^{14}C_age (years B.P.)	Error	Calendar Age (years B.P.)	1σ	Species	Reference
			GeoB 10042–1				
89145	8	3895	20	3751	65	*G. ruber, G. sacculifer*	1
98276	13	4225	40	4201	91	*G. sacculifer*	1
98279	18	4440	50	4491	89	*G. sacculifer*	1
98281	23	4580	15	4670	124	*G. sacculifer*	1
98284	33	4675	45	4798	81	*G. sacculifer*	1
98288	38	4885	20	5078	78	*G. sacculifer*	1
98291	43	5015	25	5259	67	*G. sacculifer*	1
103693	100	6130	45	6460	76	*G. ruber, G. sacculifer*	2
127996	163	7740	60	8108	82	*G. ruber, G. sacculifer*	2
103694	200	8440	50	8917	89	*G. ruber, G. sacculifer*	2
130252	213	8885	45	9460	49	*G. ruber, G. sacculifer*	2
130253	238	11830	60	13223	74	*G. ruber, G. sacculifer*	2
127997	243	13065	30	14909	140	*G. ruber, G. sacculifer*	2
130254	263	13760	60	15949	120	*G. ruber, G. sacculifer*	2
103695	300	16620	90	19454	139	*G. ruber, G. sacculifer*	2
103696	400	24210	130	27797	113	*G. ruber, G. sacculifer*	2
103698	470	30750	750	34286	677	*G. ruber, G. sacculifer*	2
103700	500	32390	660	35834	712	*G. ruber, G. sacculifer*	2
			GeoB 10043–3				
89142	13	545	35	84	59	*G. ruber, G. sacculifer*	1
89143	18	640	35	177	70	*G. ruber, G. sacculifer*	1
98502	23	1150	25	627	37	*G. sacculifer*	1
98506	28	1570	35	1029	62	*G. ruber*	1
98508	33	2070	25	1539	65	*G. sacculifer*	1
98510	38	2240	15	1741	59	*G. sacculifer*	1
98518	43	2525	30	2076	71	*G. sacculifer*	1
98520	48	2760	30	2370	65	*G. sacculifer*	1
103701	150	6520	20	6914	64	*G. ruber, G. sacculifer*	2
103702	200	8330	70	8769	129	*G. ruber, G. sacculifer*	2
103703	223	9140	90	9767	158	*G. ruber, G. sacculifer*	2
127998	273	13265	35	15215	78	*G. ruber, G. sacculifer*	2
103705	300	15235	50	17937	95	*G. ruber, G. sacculifer*	2
127999	328	19280	45	22632	106	*G. ruber, G. sacculifer*	2
103706	367	29740	490	33321	106	*G. ruber, G. sacculifer*	2
103707	385	31140	240	34580	233	*G. ruber, G. sacculifer*	2

[a]References: (1) *Southon et al.* [2013]; (2) this study.

3.3. Stable Isotope and Mg/Ca Analyses

The cores GeoB 10042–1 and GeoB 10043–3 were sampled every 5 cm for the planktic foraminifera *G. ruber* in a strict sense in order to conduct stable oxygen isotope ($\delta^{18}O$) and Mg/Ca analyses. Approximately 30–40 individuals of *G. ruber* in a strict sense collected from the 250–355 μm size fraction were first gently cracked using glass plates, then homogenized and split. About two third of the material was used for Mg/Ca analysis, and the remaining one third was used for $\delta^{18}O$ analysis. The $\delta^{18}O$ measurements were carried out using a Finnigan MAT 251 mass spectrometer at the MARUM, University of Bremen. Long-term standard deviation of the carbonate standard is $<0.07‰$. The $\delta^{18}O$ results are reported relative to the international Pee Dee belemnite (PDB) standard.

For Mg/Ca analysis, we followed the foraminifera cleaning procedure proposed by *Barker et al*. [2003]. The samples were rinsed 5 times with de-ionized water and 2 times with methanol, with ultrasonic treatment after each rinse. In the following step, organic matter was oxidized by adding a NaOH-buffered 1%-H_2O_2 reagent to the samples and placed in a hot water bath for 10 min with a few seconds in an ultrasonic bath. After repeating this step, the samples were rinsed and transferred into new acid-cleaned vials. Then, the samples underwent a weak acid leaching (0.001 M QD HNO_3) with 30 s ultrasonic treatment after which the samples were dissolved using 0.075 M QD HNO_3, centrifuged for 10 min at 6000 rpm, and transferred into

new acid cleaned vials. Mg/Ca measurements were conducted with an Agilent 720 Inductively Coupled Plasma Optical Emission Spectrometer housed at the Department of Geosciences, University of Bremen. The Mg/Ca ratio values are reported as mmol mol^{-1}. The instrumental precision during measurement was monitored by analysis of an in-house standard solution, which was measured after every fifth sample. The average 1σ error for the Mg/Ca analyses on an external standard measured along with the analyses for cores GeoB 10042–1 and GeoB 10043–3 is 0.04 mmol/mol. Sample reproducibility based on replicate samples for GeoB 10043–3 ($n = 15$) and GeoB 10042–1 ($n = 15$) is ±0.13 mmol/mol and ±0.31 mmol/mol, respectively.

Mg/Ca ratio values were converted to temperature (T) following the equation proposed by *Anand et al.* [2003] for *G. ruber* (250–350 μm):

$$Mg/Ca = 0.38\exp^{(0.09*T)} \quad (1)$$

According to sediment trap and core top studies by *Mohtadi et al.* [2007, 2009, 2011b], *G. ruber* in a strict sense records mean annual mixed layer conditions between 0 and 30 m and the dissolution effect on this species is negligible in the study area. This finding is supported by the presence of aragonitic pteropods throughout our cores that further declines any significant role of calcite dissolution in altering the primary signal preserved in the planktic foraminifera shells. Surface sediment and culture studies have shown a significant effect of salinity on the Mg/Ca ratio of planktic foraminifera shells [e.g., *Kisakürek et al.,* 2008; *Mathien-Blard and Bassinot*, 2009; *Arbuszewski et al.,* 2010]. However, the effect of salinity remains a matter of debate due to the overriding effect of dissolution [see, e.g., *Hertzberg and Schmidt*, 2013], lack of in situ measurements or unrealistic laboratory conditions. Core top studies suggest that shell Mg/Ca of planktic foraminifera is biased only in hypersaline conditions when salinity surpasses 36 psu [*Ferguson et al.,* 2008; *Gibbons et al.,* 2014], an out of reach threshold for the rain-laden eastern tropical Indian Ocean.

The stable oxygen isotope composition of foraminifera calcite is a function of temperature and the isotopic composition of the ambient seawater ($\delta^{18}O_{sw}$). In order to calculate the seawater $\delta^{18}O$ ($\delta^{18}O_{sw}$), we used the $\delta^{18}O$-temperature equation of *Bemis et al.* [1998]:

$$T(°C) = 14.9 - 4.8\left(\delta^{18}O_{cc} - \delta^{18}O_{sw}\right) \quad (2)$$

where $\delta^{18}O_{cc}$ and T are the measured $\delta^{18}O$ of calcite and Mg/Ca-based temperature, respectively. The values were then converted to standard mean ocean water (SMOW) and corrected for sea level changes as proposed by *Waelbroeck et al.* [2002]. The errors of the Mg/Ca-based temperature and $\delta^{18}O_{sw}$ reconstructions are estimated by propagating the errors introduced by *Mohtadi et al.* [2014]. The resulting errors for temperature and $\delta^{18}O_{sw}$ are on average ~1°C and 0.3‰, respectively.

3.4. X-Ray Fluorescence Core Scanning

We used the X-Ray fluorescence (XRF) Core Scanner 1 at the MARUM, University of Bremen, to perform measurements on both cores, GeoB 10042–1 and GeoB 10043–3, in 1 cm resolution. The scanner uses a KEVEX Psi Peltier Cooled Silicon Detector and a KEVEX X-ray Tube 52500008–02 with the target material molybdenum (Mo). In this study we use the elemental ratio of titanium to calcium (Ti/Ca; logarithmic scale) as a proxy to detect past changes in terrestrial input [*Mohtadi et al.,* 2010a, 2010b] to our sites GeoB 10042–1 and GeoB 10043–3.

3.5. Spliced Records and Published Data

The age-depth models for both cores were generated with a Bayesian approach using the Bacon software [*Blaauw and Christen*, 2011]. This method divides a core into sections and models the accumulation rate for each of these sections (Figure 2). Afterward we generated a spliced record for each proxy in both cores by averaging data in 500 year, nonoverlapping bins and will refer to the spliced records when discussing our results.

By comparing our record to the other published data from the eastern tropical Indian Ocean by *Levi et al.* [2007] and *Gibbons et al.* [2014], we recalculated SST and $\delta^{18}O_{sw}$ in those records by applying equations (1) and (2). Thus, the resulting values differ from those in the original publications. The binned data were then generated using the same method described above.

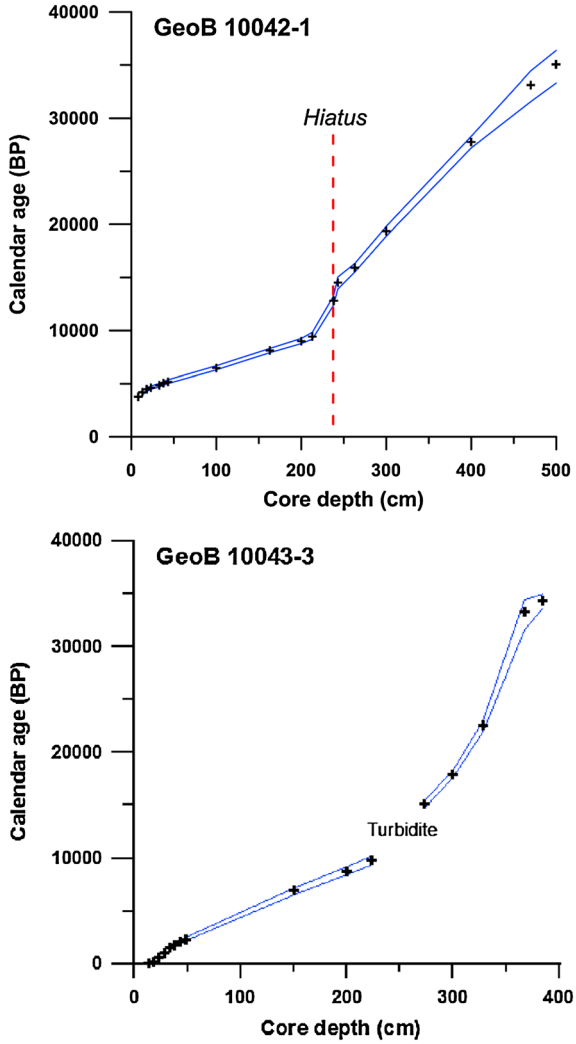

Figure 2. Age-depth model of the (top) GeoB 10042–1 and (bottom) GeoB 10043–3. The turbidite layer in GeoB 10043–3 is between 225 and 232 cm. Blue lines in both age models denote the envelope of 2σ errors. Dashed red line indicates the position of a hiatus.

4. Results

4.1. Age Model

The age models for sediment cores GeoB 10042–1 and GeoB 10043–3 are based on 18 and 16 calibrated radiocarbon dates, respectively, measured on the mixed layer dwelling planktic foraminifera species *G. ruber* and/or *Globigerinoides sacculifer* (Table 1; Figure 2). The upper 50 cm of both cores spans the last 5.2 kyr (GeoB 10042–1) and 2.3 kyr (GeoB 10043–3) have previously been studied by *Southon et al.* [2013]. In this study we provide 11 (GeoB 10042–1) and 8 (GeoB 10043–3) new radiocarbon dates.

The resulting age-depth models suggest that cores GeoB 10042–1 and GeoB 10043–3 cover the past 39.4 and 34.4 kyr and indicate that the average sedimentation rates of cores GeoB 10042–1 and GeoB 10043–3 are 23.4 cm kyr^{-1} and 16.4 cm kyr^{-1}. Both sediment cores have a distinct ash layer (GeoB 10043–3: 13–18 cm; GeoB 10042–1: 6–8 cm core depth) that has been linked to the Krakatau eruption in 1883 [*Southon et al.*, 2013]. In addition, another ash layer is observed in core GeoB 10043–3 at a depth between 370 and 382 cm and in core GeoB 10042–1 at 470 cm (Figure 3).

Both cores reveal low glacial sedimentation rates ranging between 3.4 and 19 cm kyr^{-1} (GeoB 10042–1) and between 3.1 and 11.9 cm kyr^{-1} (GeoB 10043–3) compared to the much higher Holocene sedimentation rates of 14.7 to 54.3 cm kyr^{-1} (GeoB 10042–1) and of 9.7 to 33.7 cm kyr^{-1} (GeoB 10043–3). Using the age-depth model of GeoB 10042–1, we found a hiatus indicated by a dramatic increase in the sedimentation rate from 3.6 to 31 cm kyr^{-1} around 10 kyr B.P. associated with abrupt changes in $\delta^{18}O$ and Ti/Ca log ratio (Figure 3).

4.2. Shell $\delta^{18}O$ and Mg/Ca Ratio of *G. ruber* in a Strict Sense

The $\delta^{18}O$ values of *G. ruber* in a strict sense from cores GeoB 10042–1 and GeoB 10043–3 display a similar variability over the time they overlap (Figures 3 and 4a). In the following, the last glacial and the Holocene always refer to periods >10 kyr B.P. and <10 kyr B.P., respectively. Average last glacial $\delta^{18}O$ values of GeoB 10042–1 and GeoB 10043–3 are −0.92‰ and −0.96‰, and average $\delta^{18}O$ values during the Holocene are −2.34‰ (GeoB 10042–1) and −2.46‰ (GeoB 10043–3). During the last glacial, the average values of Mg/Ca ratio for both cores are 3.58 mmol mol^{-1} (GeoB 10042–1) and 3.78 mmol mol^{-1} (GeoB 10043–3) (Figures 3 and 4b). The averages Mg/Ca ratio values of both cores during the Holocene are 4.18 (GeoB 10042–1) and 4.22 mmol mol^{-1} (GeoB 10043–3). Estimated Mg/Ca-based SSTs recorded in both sediment cores show a similar pattern for the past ~40 kyr (Figure 4b). During the last glacial, average SSTs for cores GeoB 10042–1 and GeoB 10043–3 are 24.9°C and 25.5°C (Figure 4c). During the Holocene, both SSTs show

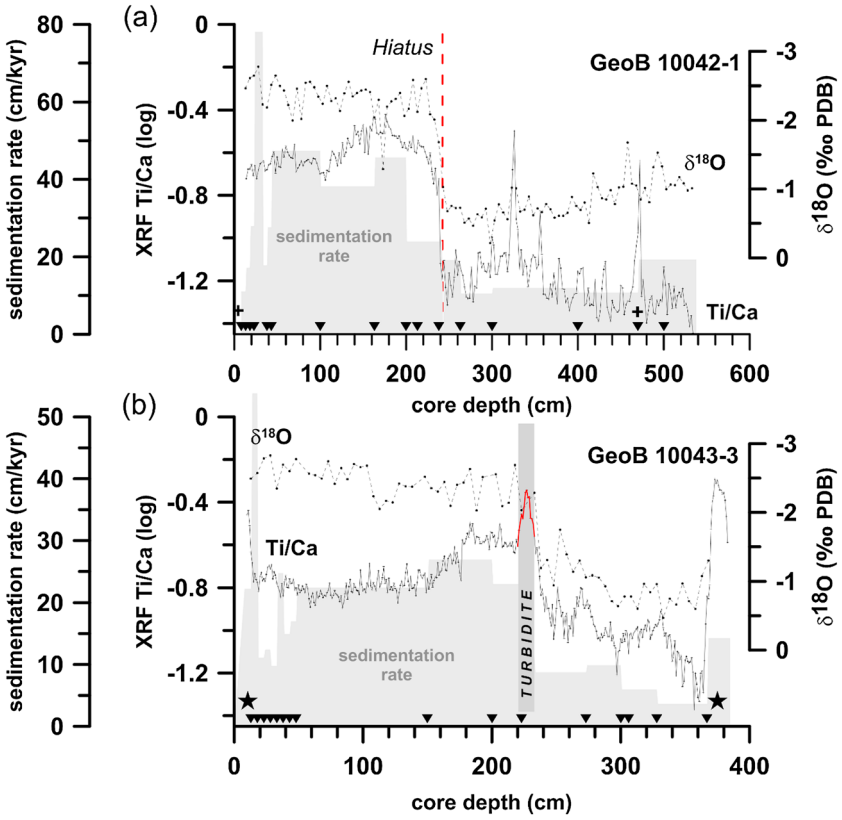

Figure 3. (a) Sedimentation rates (shaded area), $\delta^{18}O$ (dashed line), and Ti/Ca ratio (solid line) of GeoB 10042–1. Crosses denote the positions of volcanic ash layers at 5 cm and 470 cm. The dashed red line shows the position of a hiatus. Triangles indicate AMS ^{14}C dating points. (b) Same as Figure 3a but for GeoB 10043–3. Black stars depict the locations of volcanic ash layer at 10–12 cm and 370–382 cm. The red line and shaded bar show the position of the turbidite layer.

similar, slightly warmer average values of 26.6°C (GeoB 10042–1) and 26.7°C (GeoB 10043–3). Deglacial warming of 2–3°C reached maximum values during the early Holocene at around 9 kyr B.P. Subsequently, SSTs decreased by about 1°C between 9 and 7 kyr B.P. followed by a slight increase toward the present.

4.3. Seawater $\delta^{18}O$ ($\delta^{18}O_{sw}$)

During the last glacial, the average $\delta^{18}O_{sw}$ values of GeoB 10042–1 and GeoB 10043–3 are almost identical within the error, i.e., 0.65‰ and 0.69‰ (Figures 3 and 4d). Likewise, similar average $\delta^{18}O_{sw}$ values of 0.26‰ (GeoB 10042–1) and 0.23‰ (GeoB 10043–3) are observed for the Holocene. In GeoB 10043–3, $\delta^{18}O_{sw}$ values remain stable during the course of the last deglaciation until the Younger Dryas (12.8–11.5 kyr) when there is a marked increase, whereas the $\delta^{18}O_{sw}$ record of GeoB 10042–1 reveals a ~0.5‰ increase during the early deglaciation.

4.4. XRF Measurements

In general, both sediment cores indicate similar first order variability in the Ti/Ca log ratio during the past ~40 kyr (Figures 3 and 4e). In both sediment cores the Ti/Ca log ratios are much lower during the last glacial compared to the Holocene. The peak of the Ti/Ca log ratio occurred during the early Holocene. The Ti/Ca log ratios in both cores GeoB 10042–1 and GeoB 10043–3 show a declining trend from the early to mid-Holocene (8–4 kyr B.P.) followed by a slight increase afterward.

5. Discussion

5.1. Hydrologic Conditions off the Sunda Strait Prior To the Sunda Shelf Flooding (10 kyr B.P.)

During the last glacial, SST variability off the Sunda Strait (Figure 5a) is similar to other Mg/Ca-based SST reconstructions from the eastern tropical Indian Ocean (Figures 5b and 5c) [*Mohtadi et al.*, 2010a, 2014;

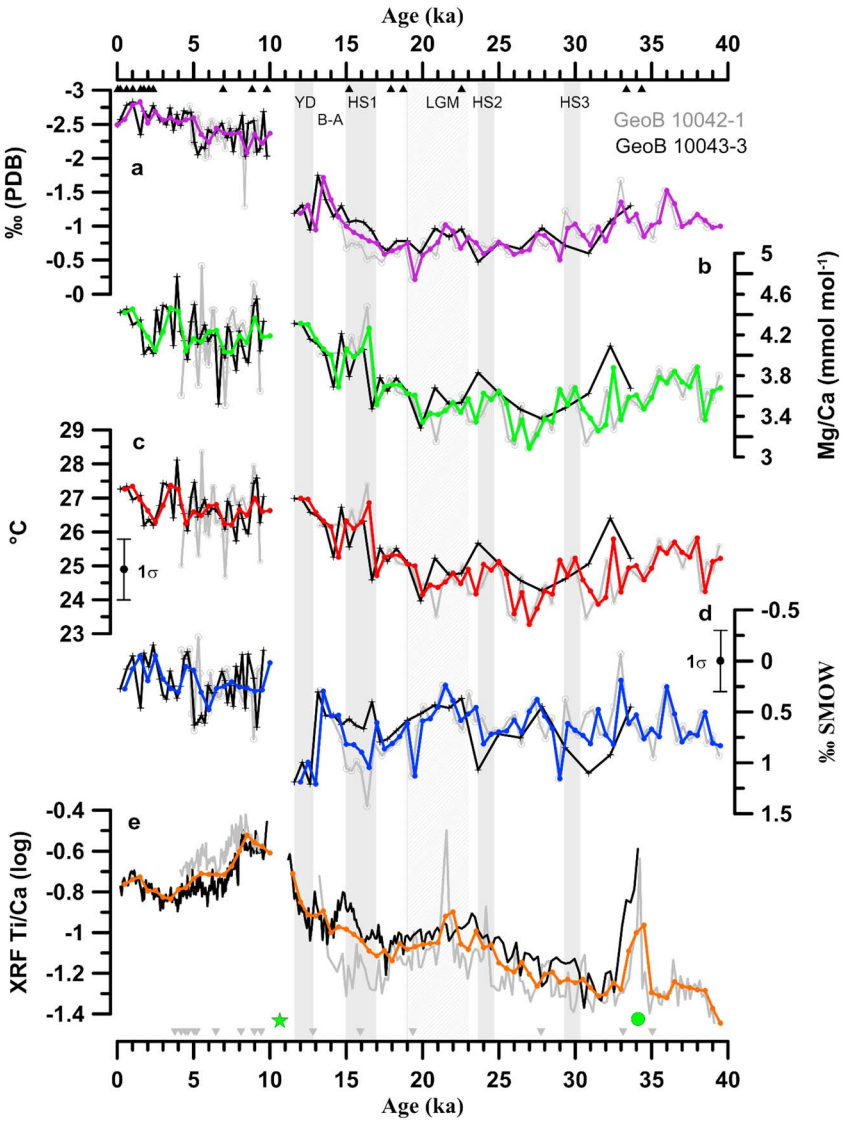

Figure 4. (a) *G. ruber* in a strict sense $\delta^{18}O$, (b) *G. ruber* in a strict sense Mg/Ca ratio, (c) SST calculations based on Figure 4b, (d) $\delta^{18}O_{sw}$ calculated from Figures 4a and 4c, and (e) Ti/Ca (logarithmic scale) of the GeoB 10042–1 (gray) and GeoB 10043–3 (black). Purple, green, red, blue, and orange curves are splice records of Figures 4a–4e. Black (grey) triangles denote AMS ^{14}C dating points for the GeoB 10043–3 (GeoB 10042–1). Shaded bars indicate LGM, Heinrich stadials (HS) 1–4, and the Younger Dryas (YD). Green stars and the green dot denote the positions of turbidite and volcanic ash layers, respectively.

Levi et al., 2007; *Xu et al.,* 2008]. Furthermore, short-term variations in our SST reconstructions are within the range of SST variability described for the upwelling region covering the south Sumatra-Java-Lesser Sunda Island chain region (between ~23° and 29°C). Reconstructed SSTs from the nonupwelling region off north and central Sumatra are 2–3°C warmer, ranging from ~25° to 30°C [*Mohtadi et al.,* 2014] (Figure 5c). Within our age model uncertainty (Figure 2), the onset of deglacial SST warming in our records (~17–18 kyr B.P.) coincides with warming over Antarctica [*Jouzel et al.,* 2007] and the atmospheric CO_2 rise [*Monnin et al.,* 2001], in line with other records of the eastern tropical Indian Ocean [*Levi et al.,* 2007; *Xu et al.,* 2008; *Mohtadi et al.,* 2010a, 2014; *Gibbons et al.,* 2014].

In order to better reconstruct the hydroclimate conditions off the Sunda Strait, we suggest Ti/Ca values reflect terrigenous input and continental runoff, where high Ti/Ca values indicate increased runoff [e.g., *Mohtadi et al.,* 2010b, 2011a] (Figure 6e). Ideally, there should be an inverse relationship between Ti/Ca and $\delta^{18}O_{sw}$ if both parameters are controlled by changes in rainfall and P-E. However, the overall increasing trend in

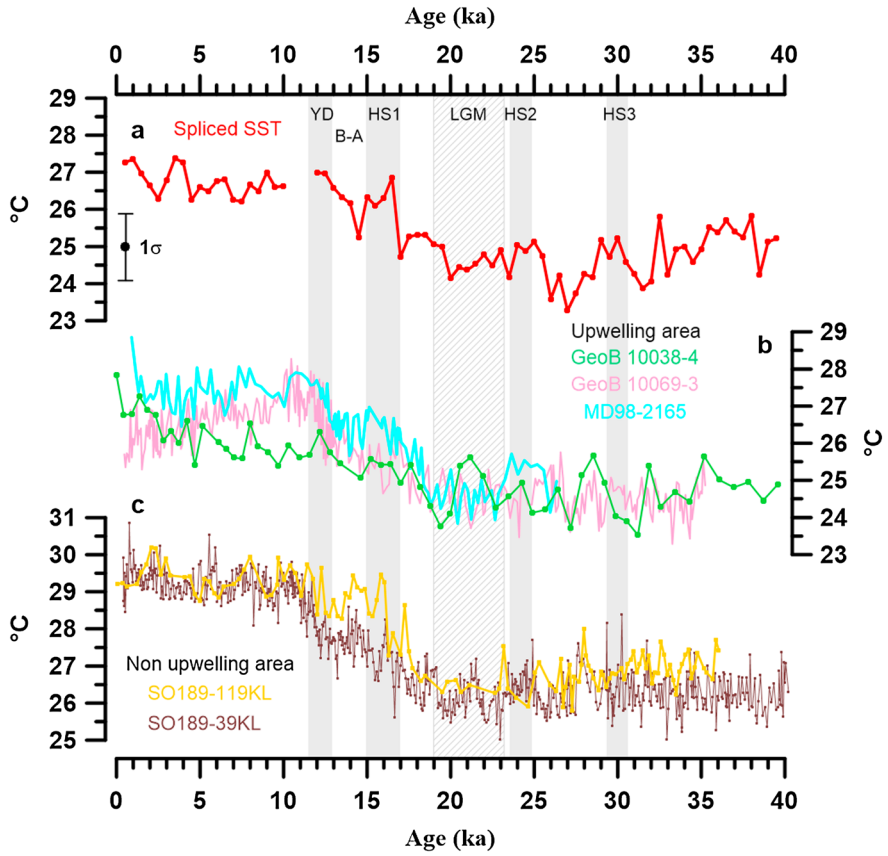

Figure 5. (a) Spliced SST record of the Sunda Strait. (b) Mg/Ca-based SSTs of GeoB 10038–4 (green curve [*Mohtadi et al.,* 2010a], of GeoB 10069–3 (pink curve] [*Gibbons et al.,* 2014], and of MD98-2165 (light blue curve) [*Levi et al.,* 2007]. (c) Mg/Ca-based SSTs of SO189-39KL (brown curve) and SO189-119KL (yellow curve) [*Mohtadi et al.,* 2014]. Shaded bars indicate LGM, Heinrich stadials (HS) 1–4, and the Younger Dryas (YD). Error bar indicates 1σ error (1°C).

Ti/Ca indicative of increasing terrigenous input during the last glacial (Figure 6e) is not paralleled by any trend in our reconstructed glacial $\delta^{18}O_{sw}$ (Figure 6a). This mismatch is not unexpected as Ti/Ca and runoff in this region include a strong seasonal signal caused by monsoonal precipitation during the NWM from December to March [*Mohtadi et al.,* 2009, 2010b, 2011a]. In contrast, results from sediment surface samples and a nearby sediment trap suggest that Mg/Ca ratio in *G. ruber* reflects mean annual surface conditions [*Mohtadi et al.,* 2009, 2011b]. Thus, our reconstructed $\delta^{18}O_{sw}$ is interpreted to reflect a mixed signal of the monsoon and nonmonsoon seasons. Besides the potential bias introduced by the different seasonality of the two sets of data, it is likely that $\delta^{18}O_{sw}$ off the Sunda Strait is additionally controlled by varying intrusion of saltier waters from below during the SEM upwelling season. Variability in $\delta^{18}O_{sw}$ in this region is also influenced by the changing direction of the South Java Current during different seasons (see section 2, study area). In summary, while the $\delta^{18}O_{sw}$ records from the more enclosed, nonupwelling basins in west and northwest of Sumatra are likely to reflect P-E in the past [*Mohtadi et al.,* 2014], *G. ruber*-based $\delta^{18}O_{sw}$ reconstructions off southwest Sumatra and from the monsoon-influenced region in Indonesia, characterized by seasonal upwelling and changing surface current directions, should be interpreted with caution as a proxy for changing rainfall or P-E.

Within the age uncertainty of our records during the last glacial, $\delta^{18}O_{sw}$ values increase during the Heinrich stadials and the Younger Dryas (Figure 6a) accompanied by a slight SST increase of 1–2°C (Figure 5a) that has been also observed in other $\delta^{18}O_{sw}$ and SST records from both the nonupwelling areas (Figures 5c and 6c) and upwelling areas (Figures 5b and 6b) of the eastern tropical Indian Ocean [*Levi et al.,* 2007; *Mohtadi et al.,* 2010a, 2014; *Gibbons et al.,* 2014]. This finding suggests widespread changes in the Indonesian hydroclimate during the millennial-scale cold periods of the Northern Hemisphere and supports previous inferences of a

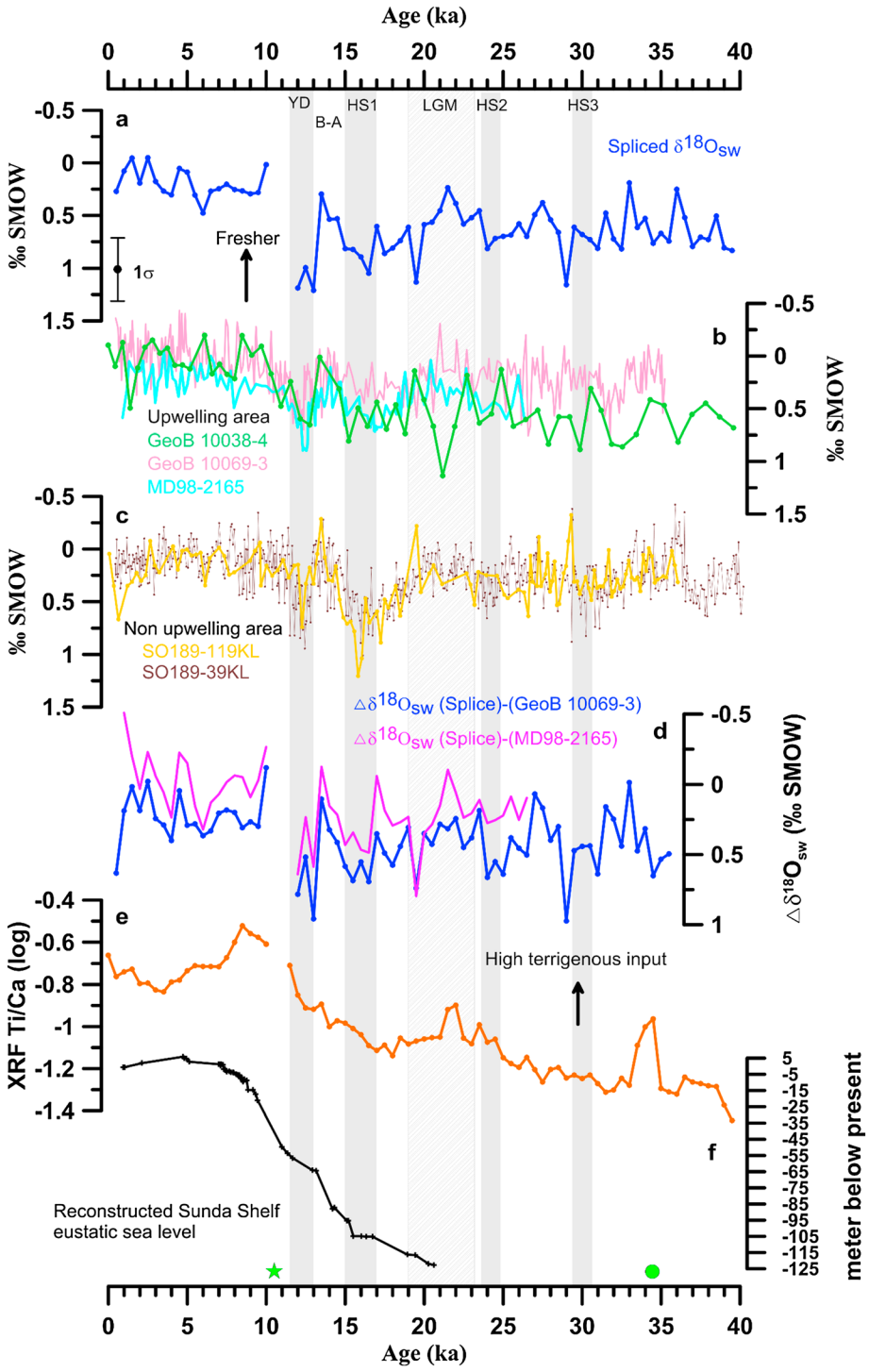

Figure 6. (a) Spliced $\delta^{18}O_{sw}$ record of the Sunda Strait (‰ SMOW). (b) *G. ruber* $\delta^{18}O_{sw}$ (‰ SMOW) of GeoB 10038–4 (green curve) [*Mohtadi et al.,* 2010a], of GeoB 10069–3 (pink curve) [*Gibbons et al.,* 2014], and of MD98-2165 (light blue curve) [*Levi et al.,* 2007]. (c) *G. ruber* $\delta^{18}O_{sw}$ (‰ SMOW) of SO189-39KL (brown curve) and SO189-119KL (yellow curve) [*Mohtadi et al.,* 2014]. (d) $\delta^{18}O_{sw}$ difference ($\Delta\delta^{18}O_{sw}$; 500 year average) between the Sunda Strait and the Savu Sea (blue curve) and between the Sunda Strait and Sumba (magenta curve). (e) Spliced record of Ti/Ca from XRF measurement (logarithmic scale). (f) Reconstructed sea level fluctuation of the Sunda Shelf [*Hanebuth et al.,* 2011]. Shaded bars indicate LGM, Heinrich stadials (HS) 1–4, and the Younger Dryas (YD). The green stars and green dot denote the positions of turbidite and volcanic ash layers, respectively. Error bar indicates 1σ error (0.3‰).

modified atmospheric circulation in the topics. Model simulations suggest a weakened and easterly displaced Hadley Circulation as a response to a weak Atlantic Meridional Overturning Circulation [*Zhang and Delworth*, 2005] or a reorganization of the Hadley Circulation and a southward displacement of the ITCZ [*Gibbons et al.,* 2014; *Mohtadi et al.,* 2014]. Further support for a southward displacement of the ITCZ during Heinrich stadials is provided by the speleothem records from the IPWP: Borneo speleothems suggest anomalous dry conditions [*Carolin et al.,* 2013], while speleothem records from Flores [*Ayliffe et al.,* 2013] and northern Australia [*Denniston et al.,* 2013] imply anomalous wet conditions during the Heinrich stadials. According to model simulations of the Heinrich stadials [*Gibbons et al.,* 2014; *Mohtadi et al.,* 2014], the eastern tropical Indian Ocean should have experienced drier and warmer conditions during the entire year, which might explain why our "mean annual" proxies of SST and $\delta^{18}O_{sw}$ record these millennial events. Therefore, the otherwise efficient control of seasonality and advection on the $\delta^{18}O_{sw}$ at our site has been minimized by an overall, year-round dry and warm eastern tropical Indian Ocean during the Younger Dryas and Heinrich stadials.

5.2. The Flooding of the Sunda Shelf

According to our results, the final (or full) opening of the Sunda Strait occurred at ~10 kyr B.P. (Figures 4–6). While in other records changes on millennial timescales are much more prominent than on glacial-interglacial scale [*Mohtadi et al.,* 2010a, 2014; *Gibbons et al.,* 2014; *Niedermeyer et al.,* 2014], our $\delta^{18}O_{sw}$ record together with that of the nearby core GeoB 10038–4 [*Mohtadi et al.,* 2010a] reveal fresher conditions since 10 kyr B.P. compared to the last glacial period (Figures 6a–6c). We attribute this freshening to the inflow of the relatively fresh Java Sea waters through the Sunda Strait at this time. Due to island topographies, almost all of the large rivers in Indonesia drain into the Java Sea and are characterized by fresher conditions compared to the surrounding seas and oceans. The opening of the Sunda Strait with shallow sill depths of only 20–40 m in the east enabled the transport of the fresh Java Sea waters to our core sites.

The spliced Ti/Ca record provides more evidence of this opening during the last deglaciation and shows a prominent change in the terrigenous material supply associated with the rapid sea level rise on the Sunda Shelf between 11 and 9.5 kyr B.P. (Figure 6f). The marked change in Ti/Ca around 10 kyr B.P. is not preserved in a sedimentary archive off south Java (*Mohtadi et al.* [2011a], not shown). The increase in Ti/Ca during this period suggests an enhanced supply of terrigenous material from the formerly exposed Sunda Shelf toward our core sites via the Sunda Strait that corresponds to the inundation of inner Sunda Shelf region at ~10.8 kyr B.P. (for details, see *Sathiamurthy and Boris* [2006] and *Hanebuth et al.* [2011]). Furthermore, sedimentation rates at both sites also indicate a marked change from ~3.5 to 31 cm kyr^{-1} (GeoB 10042–1) and from ~9.8 to 22.5 cm kyr^{-1} (GeoB 10043–3) at this time (Figure 3). This change is accompanied by a turbidite layer in core GeoB 10043–3 and a hiatus in core GeoB 10042–1 indicating possible erosive mass wasting and slope instability related to the rapid sea level rise and the opening of the Sunda Strait. After the opening, higher sedimentation rates are sustained at site closer to the Sunda Strait and support the inference of additional sediment supply through the Sunda Strait. Finally, terrigenous proxy records show an increase in kaolinite and quartz content in the nearby core BAR9442 during the Holocene that has also been related to the opening of the Sunda Strait [*Gingele et al.,* 2002].

5.3. Hydrologic Conditions Off the Sunda Strait After the Sunda Shelf Flooding

After the opening of the Sunda Strait at ~10 kyr B.P., SST varied from ~26.3° to 27.4°C. Previous studies suggest no ubiquitous Holocene SST evolution in the eastern tropical Indian Ocean region, where some suggest a clear cooling trend to the present [*Gibbons et al.,* 2014]; others interpret a continuous warming trend [*Mohtadi et al.,* 2010a, 2010b] or no trend during the Holocene [*Levi et al.,* 2007; *Xu et al.,* 2008; *Mohtadi et al.,* 2014] similar to our new data off the Sunda Strait (Figure 5). The available Holocene SST data do not reveal a distinct geographical pattern and might be additionally biased by different temporal resolutions of these records.

The Holocene $\delta^{18}O_{sw}$ records off the Sunda Strait characterizing the "open Sunda Strait setting" differ from other records from the eastern tropical Indian Ocean when comparing average glacial and interglacial values. In general lower $\delta^{18}O_{sw}$ values during the postopening compared to the preopening of the Sunda Strait indicate the permanent influence of the Java Sea waters on the hydrology at our core sites. However, the lack of correspondence between $\delta^{18}O_{sw}$ and Ti/Ca during the Holocene suggests another control on these parameters. In addition to P-E, the pattern of the Holocene Ti/Ca record is similar to the Ti/Ca record in the nearby

core GeoB 10038–4 [*Mohtadi et al.,* 2010b] and appears to follow insolation changes with maximum values during the early Holocene and minimum values at ~3 kyr B.P. This is similar to various monsoonal proxy archives that are inferred to reflect the monsoon strength during a particular season [*Dykoski et al.,* 2005; *Fleitmann et al.,* 2007; *Mohtadi et al.,* 2011a]. This trend in Ti/Ca values is not evident in the $\delta^{18}O_{sw}$ record (as discussed in section 5.1) and may reflect differences in the seasonality of these two proxies and other hydrographic controls on seawater $\delta^{18}O$.

5.4. The Impact of the Sunda Strait Opening on Regional Hydrography

The contrast between our proxy records off the Sunda Strait and those in other eastern tropical Indian Ocean records on glacial-interglacial timescales suggesting an overriding control of sea level-related changes on the hydrology off the Sunda Strait. Present day sea surface conditions in the eastern tropical Indian Ocean off the Sunda Strait are always fresher than the Lombok basin off Sumba and the Savu Sea further to the east by ~1 psu (Figure 1). To track this difference over the past ~40 kyr, we calculated the $\delta^{18}O_{sw}$ difference ($\Delta\delta^{18}O_{sw}$) between the Sunda Strait and the Savu Sea (GeoB 10069–3; blue curve in Figure 6d) and between the Sunda Strait and the Sumba area (MD98-2165; magenta curve in Figure 6d). During the Holocene, the $\delta^{18}O_{sw}$ values are indistinguishable within error. During the last glacial, there is a difference between the Sunda Strait sites and the other eastern tropical Indian Ocean sites related to the larger glacial $\delta^{18}O_{sw}$ values off the Sunda Strait (Figure 6a) compared to the glacial $\delta^{18}O_{sw}$ values at other sites that remained stable (Figures 6b and 6c). During the last glacial, $\delta^{18}O_{sw}$ values in the Savu Sea are fresher than elsewhere, possibly due to the position of the Savu Sea record sits near the major exit passage of the relatively fresh ITF (Figure 6b). This is also shown in the $\Delta\delta^{18}O_{sw}$ contrast between the Sunda Strait and Savu Sea that has been larger than the average difference between the Sunda Strait and the Lombok Basin off Sumba over the past 40 kyr (Figure 6d).

Model simulations of the LGM climate suggest that the exposure of the Sunda Shelf resulted in cooling over the Maritime Continent that weakened the Walker Circulation over the Indian Ocean and led to a stronger upwelling in the eastern tropical Indian Ocean [*DiNezio et al.,* 2011; *DiNezio and Tierney*, 2013]. However, available proxy records of past upwelling and productivity in the eastern tropical Indian Ocean do not support strong upwelling in our study area during the last glacial [*De Deckker and Gingele*, 2002; *Lückge et al.,* 2009; *Mohtadi et al.,* 2010b]. Whether the higher glacial $\delta^{18}O_{sw}$ values off the Sunda Strait reflect stronger upwelling of deeper and saltier waters in this region or a stronger influence of the saltier surface Indian Ocean is not known, and will require additional reconstructions of water mass distributions and upwelling histories for the eastern tropical Indian Ocean. It is important to note that differences between $\delta^{18}O_{sw}$ values at different locations are greatest during Heinrich stadials and the Younger Dryas even though the pattern of change in individual records is generally similar (Figure 6d, increasing $\delta^{18}O_{sw}$). This suggests a stronger zonal gradient in the hydrological cycle of the eastern tropical Indian Ocean during these times that might reflect changes in the atmospheric circulation (Walker and Hadley circulation and the position of the ITCZ, see above and *DiNezio and Tierney* [2013], *Gibbons et al.* [2014], and *Mohtadi et al.* [2014]). Overall, it is not clear to what degree different mechanisms were responsible for the similarities between proxy records from various eastern tropical Indian Ocean sites during the Holocene. Nevertheless, our data indicate that the opening of the Sunda Strait at ~10 kyr B.P. was a major control on these records, as the fresher Java Sea waters and the resulting fresh water cap introduced into the eastern tropical Indian Ocean reduced local upwelling intensity during the Holocene. Paleoproductivity reconstructions based on diatoms [*Romero et al.,* 2012] and organic carbon [*Lückge et al.,* 2009] in two cores off the Sunda Strait suggest that marine productivity during the Holocene was higher compared to the last glacial. Apparently, this higher marine productivity is due to an additional input of (terrigenous) nutrients through the Sunda Strait [*Gingele et al.,* 2002; *Mohtadi et al.,* 2010b; *Romero et al.,* 2012].

Another notable change after the opening of the Strait is a decrease in thermocline temperatures recorded in a nearby core off the Sunda Strait [*Mohtadi et al.,* 2010b]. It is possible that the opening of the Sunda Strait and the subsequent addition of freshwater to this area facilitated the development of the barrier layer (see section 2 for details) and a diverging evolution of the thermocline and surface temperatures during the Holocene. The degree to which this freshwater forcing might have been responsible for the observed changes in the upper water column has to be explored by a (transient) model-data assessment in future studies.

6. Conclusion

We have reconstructed sea surface conditions of the eastern tropical Indian Ocean off the Sunda Strait for the past 40,000 years. Our results show a major change in hydrology off the Sunda Strait with fresher conditions during the Holocene compared to the last glacial period. The surface ocean was cooler and saltier than elsewhere in the eastern tropical Indian Ocean prior to the opening of the Sunda Strait with average SST of 25°C and seawater $\delta^{18}O$ of ~0.7‰. The opening of the Sunda Strait at ~10 kyr B.P. altered surface hydrology with the inflow of low-salinity Java Sea water into the eastern tropical Indian Ocean changing average seawater $\delta^{18}O$ and SST by ~−0.5‰ and 1.7°C. Our results suggest that the opening of the Sunda Strait and the increase in terrigenous supply may have been responsible for higher marine productivity in the eastern tropical Indian Ocean during the Holocene.

Acknowledgments
We are grateful to M. Segl, B. Meyer-Schack, and S. Pape for their technical assistance. R.Y. Setiawan acknowledges financial support from the Deutscher Akademischer Austauschdienst (DAAD grant A/10/7596). This study was supported by the German Ministry of Education and Research (project PABESIA) and the Deutsche Forschungsgemeinschaft (DFG grant HE3412/15-1). The data of this study are archived and can be retrieved at PANGAEA (www.pangaea.de).

References

Aldrian, E., and R. D. Susanto (2003), Identification of three dominant rainfall regions within Indonesia and their relationship to sea surface temperature, *Int. J. Climatol.*, *23*, 1435–1452.
Anand, P., H. Elderfield, and M. H. Conte (2003), Calibration of Mg/Ca thermometry in planktonic foraminifera from a sediment trap time series, *Paleoceanography*, *18*, 1050, doi:10.1029/2002PA000846.
Arbuszewski, J., P. deMenocal, A. Kaplan, and E. C. Farmer (2010), On the fidelity of shell-derived $\delta^{18}O$ seawater estimates, *Earth Planet. Sci. Lett.*, *300*, 185–196.
Ayliffe, L. K., et al. (2013), Rapid interhemispheric climate links via the Australasian monsoon during the last deglaciation, *Nat. Commun.*, *4*, doi:10.1038/ncomms3908.
Barker, S., M. Greaves, and H. Elderfield (2003), A study of cleaning procedures used for foraminiferal Mg/Ca paleothermometry, *Geochem. Geophys. Geosyst.*, *4*, 8407, doi:10.1029/2003GC000559.
Bemis, B. E., H. J. Spero, J. Bijma, and D. W. Lea (1998), Reevaluation of the oxygen isotopic composition of planktonic foraminifera: Experimental results and revised paleotemperature equations, *Paleoceanography*, *13*, 150–160, doi:10.1029/98PA00070.
Blaauw, M., and J. A. Christen (2011), Flexible paleoclimate age-depth models using an autoregressive gamma process, *Bayesian Anal.*, *6*, 457–474.
Carolin, S. A., K. M. Cobb, J. F. Adkins, B. Clark, J. L. Conroy, S. Lejau, J. Malang, and A. A. Tuen (2013), Varied response of western pacific hydrology to climate forcings over the last glacial period, *Science*, *340*, 1564–1566.
De Deckker, P., and F. X. Gingele (2002), On the occurrence of the giant diatom Ethmodiscus rex in an 80-ka record from a deep-sea core, southeast of Sumatra, Indonesia: implications for tropical palaeoceanography, *Mar. Geol.*, *183*, 31–43.
Denniston, R. F., K.-H. Wyrwoll, Y. Asmerom, V. J. Polyak, W. F. Humphreys, J. Cugley, D. Woods, Z. LaPointe, J. Peota, and E. Greaves (2013), North Atlantic forcing of millennial-scale Indo-Australian monsoon dynamics during the Last Glacial period, *Quat. Sci. Rev.*, *72*, 159–168.
DiNezio, P. N., A. Clement, G. A. Vecchi, B. Soden, A. J. Broccoli, B. L. Otto-Bliesner, and P. Braconnot (2011), The response of the Walker circulation to Last Glacial Maximum forcing: Implications for detection in proxies, *Paleoceanography*, *26*, PA3217, doi:10.1029/2010PA002083.
DiNezio, P. N., and J. E. Tierney (2013), The effect of sea level on glacial Indo-Pacific climate, *Nat. Geosci.*, *6*, 485–491.
Ding, X., F. Bassinot, F. Guichard, Q. Y. Li, N. Q. Fang, L. Labeyrie, R. C. Xin, M. K. Adisaputra, and K. Hardjawidjaksana (2006), Distribution and ecology of planktonic foraminifera from the seas around the Indonesian Archipelago, *Mar. Micropaleontol.*, *58*, 114–134.
Du, Y., and T. Qu (2010), Three inflow pathways of the Indonesian throughflow as seen from the simple ocean data assimilation, *Dyn. Atmos. Oceans*, *50*, 233–256.
Du, Y., T. Qu, G. Meyers, Y. Masumoto, and H. Sasaki (2005), Seasonal heat budget in the mixed layer of the southeastern tropical Indian Ocean in a high-resolution ocean general circulation model, *J. Geophys. Res.*, *110*, 1978–2012, doi:10.1029/2004JC002845.
Du, Y., T. Qu, and G. Meyers (2008), Interannual variability of sea surface temperature off Java and Sumatra in a global GCM, *J. Clim.*, *21*, 2451–2465.
Dubois, N., D. W. Oppo, V. V. Galy, M. Mohtadi, S. van der Kaars, J. E. Tierney, Y. Rosenthal, T. I. Eglinton, A. Lückge, and B. K. Linsley (2014), Indonesian vegetation response to changes in rainfall seasonality over the past 25,000 years, *Nat. Geosci.*, *7*, 513–517.
Dykoski, C. A., R. L. Edwards, H. Cheng, D. Yuan, Y. Cai, M. Zhang, Y. Lin, J. Qing, Z. An, and J. Revenaugh (2005), A high-resolution, absolute-dated Holocene and deglacial Asian monsoon record from Dongge Cave, China, *Earth Planet. Sci. Lett.*, *233*, 71–86.
Ferguson, J. E., G. M. Henderson, M. Kucera, and R. E. M. Rickaby (2008), Systematic change of foraminiferal Mg/Ca ratios across a strong salinity gradient, *Earth Planet. Sci. Lett.*, *265*, 153–166.
Fleitmann, D., et al. (2007), Holocene ITCZ and Indian monsoon dynamics recorded in stalagmites from Oman and Yemen (Socotra), *Quat. Sci. Rev.*, *26*, 170–188.
Gibbons, F. T., D. W. Oppo, M. Mohtadi, Y. Rosenthal, J. Cheng, Z. Liu, and B. K. Linsley (2014), Deglacial $\delta^{18}O$ and hydrologic variability in the tropical Pacific and Indian Oceans, *Earth Planet. Sci. Lett.*, *387*, 240–251.
Gingele, X. F., P. De Deckker, A. Girault, and F. Guichard (2002), History of the South Java Current over the past 80 ka, *Palaeogeogr. Palaeoclimatol. Palaeoecol.*, *183*, 247–260.
Gordon, A. L. (2005), Oceanography of the Indonesian Seas and their throughflow, *Oceanography*, *18*(4), 14–27, doi:10.5670/oceanog.2005.01.
Gordon, A. L., R. D. Susanto, and K. Vranes (2003), Cool Indonesian Throughflow as a consequence of restricted surface layer flow, *Nature*, *425*, 824–828.
Gordon, A. L., J. Sprintall, H. M. Van Aken, D. Susanto, S. Wijffels, R. Molcard, A. Ffield, W. Pranowo, and S. Wirasantosa (2010), The Indonesian Throughflow during 2004–2006 as observed by the INSTANT program, *Dyn. Atmos. Oceans*, *50*, 115–128.
Gordon, A. L., B. A. Huber, E. J. Metzger, R. D. Susanto, H. E. Hurlburt, and T. R. Adi (2012), South China Sea throughflow impact on the Indonesian throughflow, *Geophys. Res. Lett*, *39*, L11602, doi:10.1029/2012GL052021.
Griffiths, M. L., et al. (2009), Increasing Australian-Indonesian monsoon rainfall linked to early Holocene sea-level rise, *Nat. Geosci.*, *2*, 636–639.
Griffiths, M. L., R. N. Drysdale, M. K. Gagan, J.-X. Zhao, J. C. Hellstrom, L. K. Ayliffe, and W. S. Hantoro (2013), Abrupt increase in east Indonesian rainfall from flooding of the Sunda Shelf ~9500 years ago, *Quat. Sci. Rev.*, *74*, 273–279.
Hanebuth, T., K. Stattegger, and P. M. Grootes (2000), Rapid flooding of the Sunda Shelf: A Late-Glacial sea-level record, *Science*, *288*, 1033–1035.

Hanebuth, T. J. J., H. K. Voris, Y. Yokoyama, Y. Saito, and J. Okuno (2011), Formation and fate of sedimentary depocentres on Southeast Asia's Sunda Shelf over the past sea-level cycle and biogeographic implications, *Earth Sci. Rev.*, *104*, 92–110.
Hebbeln, D., et al. (2006), Report and preliminary results of RV SONNE Cruise SO-184, Pabesia, Durban (South Africa) - Cilacap (Indonesia) - Darwin (Australia), July 8th–September 13th, 2005, 142 pp., Universität Bremen.
Hendon, H. H. (2003), Indonesian rainfall variability: Impacts of ENSO and local air–sea interaction, *J. Clim.*, *16*, 1775–1790.
Hertzberg, J. E., and M. W. Schmidt (2013), Refining *Globigerinoides ruber* Mg/Ca paleothermometry in the Atlantic Ocean, *Earth Planet. Sci. Lett.*, *383*, 123–133.
Jouzel, J., et al. (2007), Orbital and millennial antarctic climate variability over the past 800,000 years, *Science*, *317*, 793–796.
Kershaw, A. P., S. van der Kaars, and J. R. Flenley (2007), The Quaternary history of far eastern rainforests, in *Tropical Rainforest Responses to Climatic Change*, pp. 77–115, Springer, Berlin.
Kisakürek, B., A. Eisenhauer, F. Böhm, D. Garbe-Schönberg, and J. Erez (2008), Controls on shell Mg/Ca and Sr/Ca in cultured planktonic foraminiferan, *Globigerinoides ruber* (white), *Earth Planet. Sci. Lett.*, *273*, 260–269.
Levi, C., L. Labeyrie, F. Bassinot, F. Guichard, E. Cortijo, C. Waelbroeck, N. Caillon, J. Duprat, T. de Garidel-Thoron, and H. Elderfield (2007), Low-latitude hydrological cycle and rapid climate changes during the last deglaciation, *Geochem. Geophys. Geosyst.*, *8*, Q05N12, doi:10.1029/2006GC001514.
Linsley, B. K., Y. Rosenthal, and D. W. Oppo (2010), Holocene evolution of the Indonesian Throughflow and the western Pacific warm pool, *Nat. Geosci.*, *3*, 578–583.
Locarnini, R. A., et al. (2013), in *World Ocean Atlas 2013: Temperature*, vol. 1, edited by S. Levitus and A. Mishonov, 40 pp., NOAA Atlas NESDIS 73, Silver Spring, Md.
Lückge, A., M. Mohtadi, C. Rühlemann, G. Scheeder, A. Vink, L. Reinhardt, and M. Wiedicke (2009), Monsoon versus ocean circulation controls on paleoenvironmental conditions off southern Sumatra during the past 300,000 years, *Paleoceanography*, *24*, PA1208, doi:10.1029/2008PA001627.
Maloney, B. K. (1980), Pollen analytical evidence for early forest clearance in North Sumatra, *Nature*, *287*, 324–326.
Mathien-Blard, E., and F. Bassinot (2009), Salinity bias on the foraminifera Mg/Ca thermometry: Correction procedure and implications for past ocean hydrographic reconstructions, *Geochem. Geophys. Geosyst.*, *10*, Q12011, doi:10.1029/2008GC002353.
Mohtadi, M., L. Max, D. Hebbeln, A. Baumgart, N. Krück, and T. Jennerjahn (2007), Modern environmental conditions recorded in surface sediment samples off W and SW Indonesia: Planktonic foraminifera and biogenic compounds analyses, *Mar. Micropaleontol.*, *65*, 96–112.
Mohtadi, M., S. Steinke, J. Groeneveld, H. G. Fink, T. Rixen, D. Hebbeln, B. Donner, and B. Herunadi (2009), Low-latitude control on seasonal and interannual changes in planktonic foraminiferal flux and shell geochemistry off south Java: A sediment trap study, *Paleoceanography*, *24*, PA1201, doi:10.1029/2008PA001636.
Mohtadi, M., S. Steinke, A. Lückge, J. Groeneveld, and E. C. Hathorne (2010a), Glacial to Holocene surface hydrography of the tropical eastern Indian Ocean, *Earth Planet. Sci. Lett.*, *292*, 89–97.
Mohtadi, M., A. Lückge, S. Steinke, J. Groeneveld, D. Hebbeln, and N. Westphal (2010b), Late Pleistocene surface and thermocline conditions of the eastern tropical Indian Ocean, *Quat. Sci. Rev.*, *29*, 887–896.
Mohtadi, M., D. W. Oppo, S. Steinke, J.-B. W. Stuut, R. De Pol-Holz, D. Hebbeln, and A. Lückge (2011a), Glacial to Holocene swings of the Australian-Indonesian monsoon, *Nat. Geosci.*, *4*, 540–544.
Mohtadi, M., D. W. Oppo, A. Lückge, R. DePol-Holz, S. Steinke, J. Groeneveld, N. Hemme, and D. Hebbeln (2011b), Reconstructing the thermal structure of the upper ocean: Insights from planktic foraminifera shell chemistry and alkenones in modern sediments of the tropical eastern Indian Ocean, *Paleoceanography*, *26*, PA3219, doi:10.1029/2011PA002132.
Mohtadi, M., M. Prange, D. W. Oppo, R. De Pol-Holz, U. Merkel, X. Zhang, S. Steinke, and A. Lückge (2014), North Atlantic forcing of tropical Indian Ocean climate, *Nature*, *509*, 76–80.
Monnin, E., A. Indermühle, A. Dällenbach, J. Flückiger, B. Stauffer, T. F. Stocker, D. Raynaud, and J.-M. Barnola (2001), Atmospheric CO_2 concentrations over the Last Glacial termination, *Science*, *291*, 112–114.
Niedermeyer, E. M., A. L. Sessions, S. J. Feakins, and M. Mohtadi (2014), Hydroclimate of the western Indo-Pacific Warm Pool during the past 24,000 years, *Proc. Natl. Acad. Sci.*, *111*, 9402–9406.
Pelejero, C., M. Kienast, L. Wang, and J. O. Grimalt (1999), The flooding of Sundaland during the last deglaciation: Imprints in hemipelagic sediments from the southern South China Sea, *Earth Planet. Sci. Lett.*, *171*, 661–671.
Putri, M. R. (2005), Study of ocean climate variability (1959–2002) in the eastern Indian Ocean, Java Sea and Sunda Strait using the HAMburg Shelf Ocean model, Dissertation, Univ. Hamburg, 104 pp.
Qu, T., and G. Meyers (2005), Seasonal variation of barrier layer in the southeastern tropical Indian Ocean, *J. Geophys. Res.*, *110*, C11003, doi:10.1029/2004JC002816.
Qu, T., Y. Du, J. Strachan, G. Meyers, and J. Slingo (2005), Sea surface temperature and its variability in the Indonesian region, *Oceanography*, *18*, 50–61.
Reimer, P. J., et al. (2013), IntCal13 and Marine13 radiocarbon age calibration curves 0–50,000 years cal BP, *Radiocarbon*, *55*, 1869–1887.
Romero, O. E., M. Mohtadi, P. Helmke, and D. Hebbeln (2012), High interglacial diatom paleoproductivity in the westernmost Indo-Pacific Warm Pool during the past 130,000 years, *Paleoceanography*, *27*, PA3209, doi:10.1029/2012PA002299.
Russell, J. M., H. Vogel, B. L. Konecky, S. Bijaksana, Y. Huang, M. Melles, N. Wattrus, K. Costa, and J. W. King (2014), Glacial forcing of central Indonesian hydroclimate since 60,000 y B.P, *Proc. Natl. Acad. Sci. U.S.A.*, *111*, 5100–5105.
Sathiamurthy, E., and H. K. Voris (2006), Maps of Holocene sea level transgression and submerged lakes on the Sunda Shelf, *Nat. History J. Chulalongkorn Univ., Suppl. 2*, 1–43.
Southon, J., M. Mohtadi, and R. De Pol-Holz (2013), Planktic foram dates from the Indonesian Arc: Marine ^{14}C reservoir ages and a mythical AD 535 volcanic eruption, *Radiocarbon*, *55*, 1869–1887.
Sprintall, J., S. Wijffels, R. Molcard, and I. Jaya (2010), Direct evidence of the South Java Current system in Ombai Strait, *Dyn. Atmos. Oceans*, *50*, 140–156.
Sprintall, J., S. E. Wijffels, R. Molcard, and I. Jaya (2009), Direct estimates of the Indonesian Throughflow entering the Indian Ocean: 2004–2006, *J. Geophys. Res.*, *114*, C07001, doi:10.1029/2008JC005257.
Stuijts, I., J. C. Newsome, and J. R. Flenley (1988), Evidence for late quaternary vegetational change in the Sumatran and Javan highlands, *Rev. Palaeobot. Palynol.*, *55*, 207–216.
Susanto, R. D., A. L. Gordon, and Q. Zheng (2001), Upwelling along the coasts of Java and Sumatra and its relation to ENSO, *Geophys. Res. Lett.*, *28*, 1599–1602, doi:10.1029/2000GL011844.
Tjia, H. D. (1980), The Sunda Shelf, SE Asia, *Z. Geomorphol.*, *24*, 405–427.

van der Kaars, S., F. Bassinot, P. De Deckker, and F. Guichard (2010), Changes in monsoon and ocean circulation and the vegetation cover of southwest Sumatra through the last 83,000 years: The record from marine core BAR94-42, *Palaeogeogr. Palaeoclimatol. Palaeoecol.*, *296*, 52–78.

Vranes, K., and A. L. Gordon (2005), Comparison of Indonesian Throughflow transport observations, Makassar Strait to eastern Indian Ocean, *Geophys. Res. Lett.*, *32*, L10606, doi:10.1029/2004GL022158.

Waelbroeck, C., L. Labeyrie, E. Michel, J. C. Duplessy, J. F. McManus, K. Lambeck, E. Balbon, and M. Labracherie (2002), Sea-level and deep water temperature changes derived from benthic foraminifera isotopic records, *Quat. Sci. Rev.*, *21*, 295–305.

Wijffels, S. E., S. Hautala, G. Meyers, and W. Morawitz (1996), The WOCE Indonesian throughflow repeat hydrography sections: I10 and IR6, *Int. WOCE Newsl.*, *24*, 25–28.

Xu, J., A. Holbourn, W. Kuhnt, Z. Jian, and H. Kawamura (2008), Changes in the thermocline structure of the Indonesian outflow during Terminations I and II, *Earth Planet. Sci. Lett.*, *273*, 152–162.

Zhang, R., and T. L. Delworth (2005), Simulated tropical response to a substantial weakening of the Atlantic thermohaline circulation, *J. Clim.*, *18*, 1853–1860.

Zweng, M. M., et al. (2013), *World Ocean Atlas 2013: Salinity*, vol. 2, edited by S. Levitus and A. Mishonov, 39 pp., NOAA Atlas NESDIS 74, Silver Spring, Md.